# Enhanced pulse electrocatalytic reductive-oxidative degradation of chlorinated organic pollutants based on a synergistic effect from Pd single atoms and FeCo$_2$O$_4$ nanowire

Mengxue Li [a,b], Hui Wang [a,b,*], Shunlin Li [a,b], Wenchao Yu [a,b], Xiangting Hou [a,b], Xinyu Li [a,b], Zhaoyong Bian [c,**]

[a] Beijing Key Lab for Source Control Technology of Water Pollution, College of Environmental Science and Engineering, Beijing Forestry University, Beijing 100083, PR China
[b] Engineering Research Center for Water Pollution Source Control & Eco-remediation, College of Environmental Science and Engineering, Beijing Forestry University, Beijing 100083, PR China
[c] College of Water Sciences, Beijing Normal University, Beijing 100875, PR China

ARTICLE INFO

ABSTRACT

Targeting complete dechlorination and decomposition of chlorinated organic pollutants in an environmentally friendly and resource efficient manner. In this investigation, a three-dimensional multi-structured electrode (Pd-NC@Fe/CoCF) comprising Pd monatomic and nitrogen-doped carbon-coated FeCo$_2$O$_4$ nanowire cluster arrays were effectively synthesized. This electrode demonstrated efficient generation of H* and the production of •OH through a (2+1) e$^-$ oxygen reduction mechanism under the synergistic action of Pd single atoms and FeCo$_2$O$_4$ nanowire. When integrated with a square-wave pulsed electrocatalytic system, the chlorinated organic pollutants could be fully degraded within 45 min under the most favorable process parameters, which include a pulse voltage of −0.7 V, a duty cycle of 50 %, and a pulse frequency of 0.1 Hz. This results in a removal rate of 92.3 % for TOC and an energy consumption of 1.27 kWh·kg$^{-1}$. This study presents a sustainable and environmentally friendly approach to the electrochemical degradation of chlorinated organic pollutants.

## 1. Introduction

Chlorinated organic pollutants, such as trichloroethylene (TCE) and 1,2,4-trichlorobenzene (1,2,4-TCB), are classified as dense non-aqueous phase liquids and are commonly employed in industrial operations. The improper discharge or accidental leakage of this pollutant may pose a risk to soil and groundwater [1–3]. The worldwide apprehension about the existence of TCE and 1,2,4-TCB in the environment arises from their potential carcinogenic and toxic effects, even at low concentrations [4, 5]. Conventional methods, including biodegradation and adsorption thermal catalysis, are linked to challenges such as high costs and incomplete treatment [6–8]. The electrocatalytic degradation of chlorinated organic pollutants enables the concurrent reduction of pollutants reduction and oxidative degradation. However, the current electrocatalytic technology depends on a direct current stabilized power supply to provide the external electric field. This approach is linked to challenges such as incomplete treatment of chlorinated organic pollutants and high energy consumption, which limits the practical application of this technology. Furthermore, advanced oxidation processes (AOPs) are widely recognized as an environmentally sustainable and cost-effective technique for producing elevated levels of •OH employing the in situ production of H$_2$O$_2$. Nevertheless, they suffer from incomplete reductive dechlorination and may produce oxidation intermediates that are more harmful than the original contaminants. Hence, there is an immediate requirement to advance technologies that enable the swift and low-consumption degradation of TCE and 1,2,4-TCB through the facilitation of reduction or oxidation of TCE and 1,2,4-TCB, as well as their intermediate breakdown products.

Pulsed electrocatalysis has the potential to induce a sequence of evolutionary phases at the active site of the electrocatalyst. During the

$T_{on}$ period, chlorinated organic pollutants adsorb on the electrode surface and are eventually degraded to other substances at the electrode surface. Simultaneously, charged substances begin to accumulate near the electrode-electrolyte interface. The accumulation of charges consisting of a combination of positive charges on the surface of the electrode and positive or negative charges from the environment near the electrode results in the formation of an electric double layer (EDL) [9]. Through the addition of supplemental pulses of $E_{rest}$ and $T_{rest}$ factors can effectively decrease energy consumption and the thickness of the diffusion layer during adsorption and desorption, while also improving mass transfer and the kinetics of chlorinated organic pollutants and water electrolysis [10–15]. The application of pulsed electrocatalysis techniques has the potential to significantly improve the selectivity of electrochemical reactions, mitigate side reactions, enhance reaction efficiency, and decrease energy consumption. This phenomenon is especially noticeable in situations characterized by low levels of pollutants and a greater abundance of coexisting substances. In such cases, the pulsed power supply exhibits higher energy efficiency when compared to the constant voltage and constant current methods [16]. The pulsed electrocatalytic system provides an effective method for the degradation of chlorinated organic pollutants.

The primary component of the heterogeneous electro-Fenton (EF) process is a unified cathode that produces $H_2O_2$ in situ through the $2e^-$ oxygen reduction reaction (ORR) pathway. Subsequently, $H_2O_2$ undergoes $1e^-$ decomposition to generate •OH [17,18]. The noble metal Pd demonstrates a high level of selectivity in the $2e^-$ ORR and displays notable reducibility through electrocatalytic hydrodechlorination (EHDC) [19–21]. Nevertheless, the natural scarcity and high cost of Pd restrict large-scale commercialization, especially in water treatment practices. Single atoms (SAs) catalysts exhibit significant potential for advancement owing to their distinctive electronic properties, extremely low metal loading, nearly 100 % atom utilization efficiency, and environmentally friendly nature. Furthermore, $FeCo_2O_4$ has been identified as a highly effective spinel-structured catalyst possessing various oxidation states, remarkable stability, and dielectric properties [22,23]. This catalyst has demonstrated the ability to effective in degrading 2, 4-dichlorophenol and atrazine [24]. The fabrication of bimetallic nanowire cluster arrays (NWCAs) prevents metal aggregation, thereby facilitating the full exposure of active sites and ensuring rapid electron transfer during catalytic reactions. They demonstrate superior kinetic performance and efficiency in the degradation of various chlorinated organic pollutants [7,25–28]. To enhance the structural stability of NWCAs, it is possible to apply a protective layer to the surface [29]. Nitrogen-doped carbon (NC) films exhibit favorable stability and conductivity, enabling the dispersion of metal catalysts, reduction of metal particle cohesion, and influence on the electronic effect, and enhancing the adsorption of pollutants. Despite the abundance of literature on Pd SAs and NWCAs based materials, there remains a dearth of comprehensive understanding regarding the reaction sites and mechanisms of single atom loaded NWCAs for dechlorination. Therefore, an extensive and systematic study is warranted.

In this study, a three-dimensional multi-structured electrode material Pd-NC@Fe/CoCF was developed through the utilization of NC film-coated $FeCo_2O_4$ NWCAs anchored on copper foam (CF) with Pd SAs. The individual Pd atoms' atomic dispersion and coordination structures were verified through aberration-corrected high-angle annular dark field scanning transmission electron microscopy (AC-HAADF-STEM) and X-ray absorption fine structure (XAFS) measurements. The Pd-NC@Fe/CoCF electrode facilitated the reductive dechlorination and oxidative decomposition of chlorinated organic pollutants through pulsed electrocatalysis. The current investigation emphasizes the pulsed electrocatalytic degradation of chlorinated organic pollutants through the production of H* at the electrode surface and the highly selective generation of $H_2O_2$ activation to •OH by the collaborative interplay of Pd SAs and $FeCo_2O_4$ NWCAs, resulting in a low-cost and efficient degradation of pollutants.

## 2. Materials and methods

### 2.1. Synthesis of Pd-NC@Fe/CoCF

This material was produced using an improved version of a previously published method [30]. For the hydrothermal method, cobalt nitrate hexahydrate $(Co(NO_3)_2 \cdot 6\,H_2O)$, ferric nitrate nonahydrate $(Fe(NO_3)_3 \cdot 9\,H_2O)$, ammonium fluoride $(NH_4F)$, and urea $(CO(NH_2)_2)$ were dissolved separately in 30 mL of deionized water. Subsequently, the resulting solution and CF were transferred into the 50 mL high-pressure hydrothermal reactor and kept at 120°C for 8 h. The CF, coated with a pink product, was then removed from the autoclave. Upon electro-polymerization of the polypyrrole film on the electrode surface. The electrode was subsequently subjected to calcination at 400°C for 1 h in a nitrogen $(N_2)$ atmosphere, resulting in the formation of NC@Fe/CoCF. Immersed the electrode was submerged in a specific concentration of palladium chloride $(PdCl_2)$ solution and dried in a vacuum drying oven at 60°C. Subsequently, the electrode was calcined at 900°C for 1 h in an $N_2$ atmosphere to obtain Pd-NC@Fe/CoCF. The preparation process is depicted in Fig. 1a. Preparation of Pd-NCF under the same preparation conditions. Text S1 offers supplementary information regarding the materials utilized in the fabrication of the catalyst.

### 2.2. Characterization of materials

X-ray diffraction (XRD) patterns were obtained using a Shimadzu XRD-7000 diffractometer with Cu Kα radiation over the 10°–80° range [31]. High-resolution X-ray photoelectron spectroscopy (XPS) was conducted utilizing an ESCALAB 250Xi X-ray photoelectron spectrometer with Mg KII radiation. The XPS data obtained were calibrated at the C 1 s binding energy of 284.6 eV [32]. The hydrophilicity of the electrode surface was assessed using a contact angle (CA) meter (OCA20, Germany). The X-ray absorption spectroscopy (XAS) was used to investigate the local coordination environment, including the coordination number and bond length, of the Pd atoms in Pd-NC@Fe/CoCF. The Pd K-edge spectra were obtained at beamline 14W1 of the Shanghai Synchrotron Radiation Facilities. The analysis of the extended X-ray absorption fine structure (EXAFS) data was conducted utilizing the ATHENA and AETEMIS programs within the Demeter computer package [33]. Athena software was used for XAFS data processing including conversion of raw data to μ(E) spectra, background subtraction and normalization, and Fourier transformation and plotting. Artemis software was used for analysis of EXAFS data using theoretical standards, including setting the range of the Fourier transform from K-space and fitting range parameters in R-space. Text S2 provides additional methods for characterizing materials.

### 2.3. Electrochemical measurements

Electrochemical measurements were carried out using a CHI-760E electrochemical workstation (CH Instruments, Inc., Shanghai Chenhua China) and a rotator (PINE Instruments model: AFMSRCE, USA). The three-electrode system comprised a platinum ring as the counter electrode, Ag/AgCl as the reference electrode, and a rotating ring-disk electrode (RRDE, disk area: 0.2475 $cm^2$, ring area: 0.1866 $cm^2$) as the working electrode. The selectivity of the catalysts about $H_2O_2$ formation and the number of transferred electrons at the disk electrode during the ORR were calculated using Eqs. (1)-(4), respectively [34,35]:

$$\frac{1}{J} = \frac{1}{J_L} + \frac{1}{J_k} = \frac{1}{B\omega^{1/2}} + \frac{1}{J_k} \tag{1}$$

where

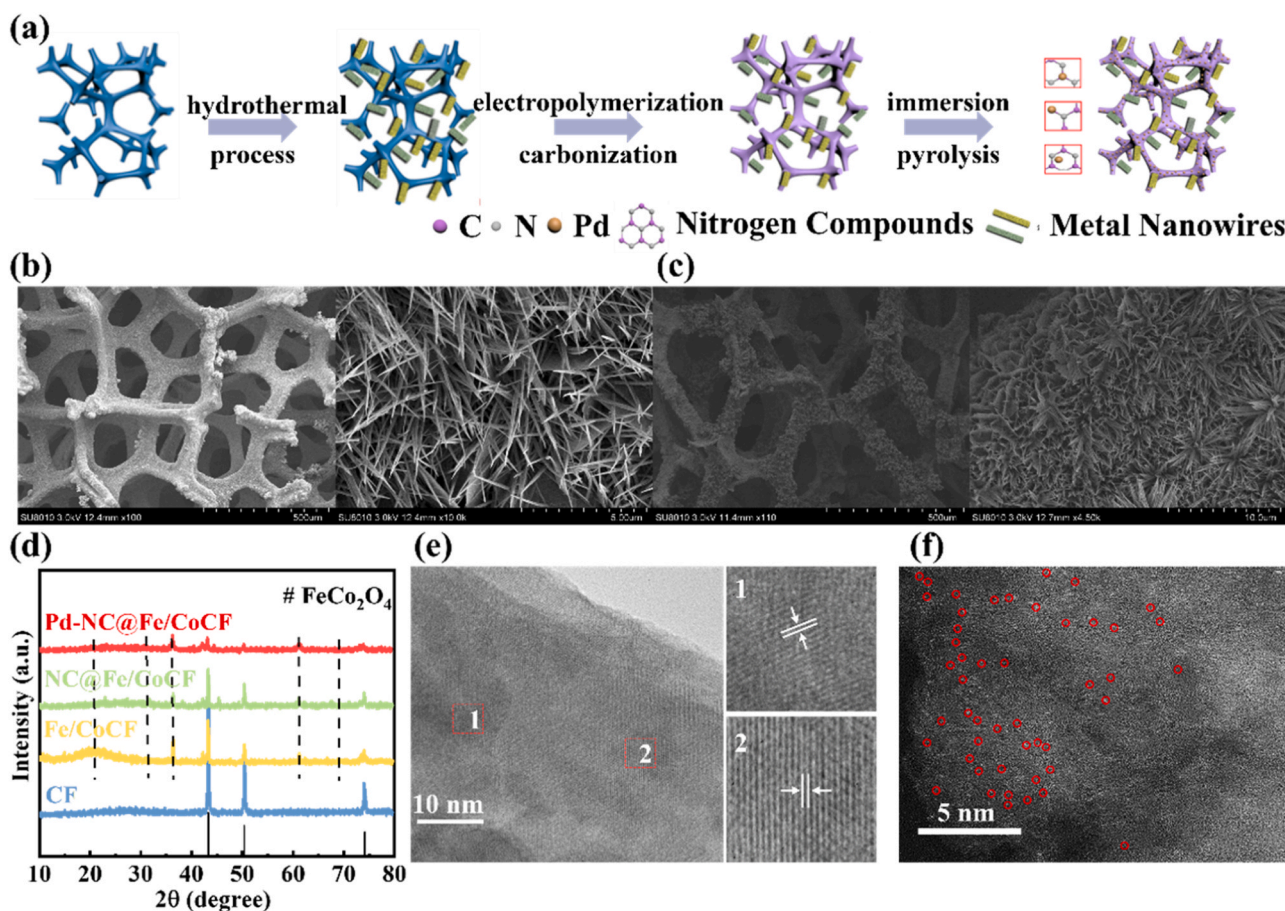$$B = 0.62nFC_0D_0^{2/3}\upsilon^{-1/6} \tag{2}$$

and

**Fig. 1.** (a) The preparation process of the Pd-NC@Fe/CoCF. (b-c) SEM images of the Fe/CoCF and Pd-NC@Fe/CoCF. (d) XRD spectra of the different catalysts. (e) TEM images of the Pd-NC@Fe/CoCF. (f) AC-HAADF-STEM images of the Pd-NC@Fe/CoCF.

$$H_2O_2\% \ = \ \frac{2I_D}{I_D + I_R/N} \ \times \ 100\% \tag{3}$$

together with

$$n \ = \ \frac{4I_D}{I_D + I_R/N} \tag{4}$$

Where, J is the measured current density (mA·cm$^{-2}$), $J_L$ is the diffusion-limited current density (mA·cm$^{-2}$), $J_k$ is the kinetic current density (mA·cm$^{-2}$), ω is the electrode rotational speed (rpm), n is the number of electron transfer, F is the Faraday constant (96485 C·mol$^{-1}$), $C_0$ is the saturation concentration of oxygen in the liquid reaction medium, and $D_0$ is the oxygen diffusion rate (1.93 × 10$^{-5}$ cm·s$^{-1}$), υ is the viscosity coefficient, $I_D$ is the disc current (mA·cm$^{-2}$), $I_R$ is the ring current (mA·cm$^{-2}$), and N is the collection coefficient of H$_2$O$_2$ at the ring (N = 0.37).

### 2.4. Dechlorination degradation analysis

The reaction solution had a volume of 50 mL, and the electrolyte consisted of 0.05 mol·L$^{-1}$ Na$_2$SO$_4$ and 0.05 mol·L$^{-1}$ DMF solution. DMF is a solubilizer for chlorinated hydrocarbons. The initial pH of the reaction solution is 7.0. A 1 mL sample is obtained near the cathode. Specific experimental steps for the dechlorination degradation were performed as described in Text S3. The data points depicted in the figures presented in this document are the means of three replicated trials and are accompanied by error bars. The degradation device diagram is shown in Fig. S1.

### 2.5. Analytical method

The levels of chlorinated organic pollutants in a solution were quantified using an Agilent 7890 A/5975 C gas chromatography-mass spectrometry (GC-MS) system equipped with an HP-5MS UI column (30 m × 0.25 mm × 0.25 μm, Agilent). The temperature was increased to 35°C and maintained for 5 min, after which the sample was heated at a rate of 8.0 °C·min$^{-1}$ until it reached 200°C, where it was held for 1 min [36,37]. The TOC content of the reaction system was analyzed using a TOC-VCSA series carbon analyzer. Electron paramagnetic resonance (EPR) spectra were acquired at room temperature using an EMXplus-10/12 instrument [38]. Isopropyl alcohol (IPA), p-benzoquinone (p-BQ), furfuryl alcohol (FFA), and tertiary butanol (t-BuOH) were used as •OH, O$_2^{\bullet-}$, $^1$O$_2$, and H* quenchers, respectively [39,40]. The specific steps used to determine the cumulative reactive oxygen species concentrations are provided in Text S4. The H$_2$O$_2$ concentration in the electrocatalytic system was assessed through spectrometry using the potassium titanyl oxalate method with a U-2910 spectrophotometer (Hitachi, Japan) [41]. And the toxicity of the intermediate products produced by the reaction was predicted by Toxicity Estimation Software Tool (T.E.S.T).

### 2.6. Theoretical calculation

The study utilized density functional theory (DFT) simulations to identify the specific sites of pollutant molecules susceptible to degrading processes, using the Gaussian 09 W and Multiwfn 3.8 software packages. Further information on the theoretical calculations is given in Text S5.

## 3. Results and discussion

### 3.1. Coordination structure and physicochemical properties of Pd-NC@Fe/CoCF

As depicted in Fig. S2, the CF exhibits a porous structure and a smooth surface. As illustrated in Figs. 1b and 1c, the Fe and Co uniformly developed into nanowire arrays on the CF. Compared with Fe/CoCF, the morphology of Pd-NC@Fe/CoCF nanowires remained largely unchanged, suggesting that the presence of NC and Pd SAs does not exert a significant influence on the nanowire morphology of the nanowires. The majority of Pd-NC@Fe/CoCF nanowires exhibit significantly larger diameters compared to Fe/CoCF, primarily attributed to the presence of NC and Pd SAs enveloping the nanowires. The EDS images of the Pd-NC@Fe/CoCF (Fig. S3) reveal a uniform distribution of the elements

C, N, O, Fe, Co, and Pd on the electrode. The XRD pattern depicted in Fig. 1d displays a peak corresponding to $FeCo_2O_4$, suggesting the presence of a spinel oxide phase on the CF. As demonstrated in Table S1, the lattice parameter of Fe/CoCF experienced a slight increase, suggesting the substitution of some Co with Fe in $Co_3O_4$. The lattice edges of Pd-NC@Fe/CoCF indicate a planar spacing of 0.385 nm, which corresponds closely to the (111) plane of the $FeCo_2O_4$ phase. Atomically-dispersed Pd centers situated on the NC may be easily seen thanks to the appearance of bright spots in the AC-HAADF-STEM picture in Fig. 1f.

The surface chemistry and molecular status of Pd-NC@Fe/CoCF were determined by XPS analysis. It is evident from the spectra in Fig. S4 that signals pertaining to C, O, N, Fe, Co, Cu, and Pd were applied to the substrate material's surface. Compared with the C element, the N element content is lower, because the binding energy of the C-N bond ($305\ kJ \cdot mol^{-1}$) is lower than that of the C-C bond ($379\ kJ \cdot mol^{-1}$).
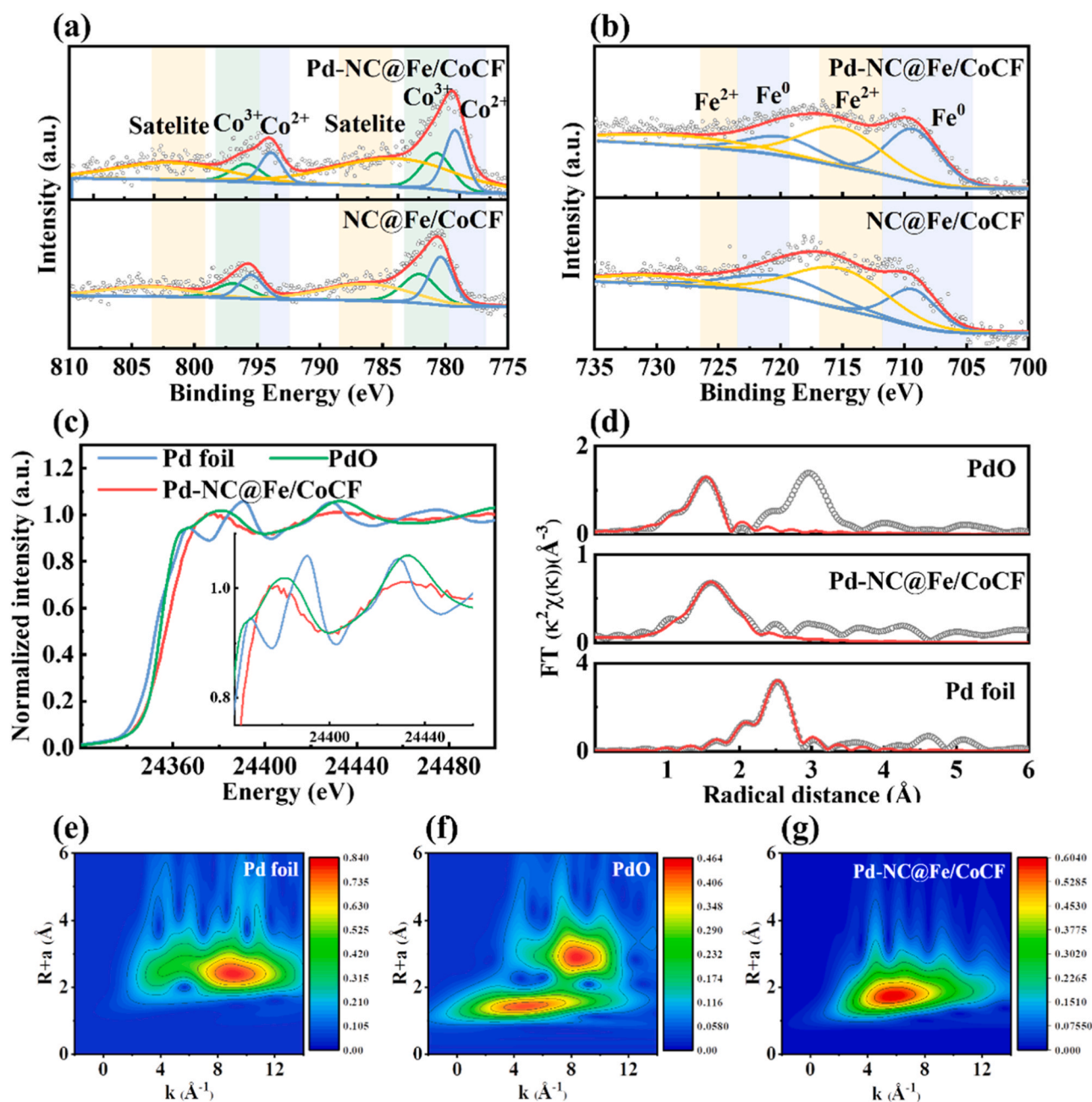


**Fig. 2.** (a) Co 2p XPS spectra of the NC@Fe/CoCF and Pd-NC@Fe/CoCF. (b) Fe 2p XPS spectra of the NC@Fe/CoCF and Pd-NC@Fe/CoCF. (c) XANES spectra of Pd-NC@Fe/CoCF and references. (d) Pd K-edge EXAFS spectrum of Pd-NC@Fe/CoCF and references. (e-g) WT-EXAFS of Pd foil, PdO, and Pd-NC@Fe/CoCF.

During pyrolysis at high temperatures, the C-N bond is more fragile, and the rearrangement of the carbon skeleton leads to the breakage of the C-N bond, resulting in partial N loss (Table S2). The high-resolution spectra of the Co 2p are depicted in Fig. 2a. Two principal peaks coincide with the spin-orbit peaks of Co $2p_{3/2}$ and Co $2p_{1/2}$, respectively, and are located at around 779.8 and 795.0 eV. The fitting indicates that the peaks at around 779.5 and 794.6 eV are related to $Co^{3+}$, whereas the peaks at 781.4 and 796.5 eV, in addition to their satellite peaks, are related to $Co^{2+}$ [42,43]. The Pd-NC@Fe/CoCF nanowire has a $Co^{3+}/Co^{2+}$ ratio of 1.15, as determined by the overlapping peak regions. This ratio indicates a higher exposure of $Co^{3+}$ atoms on the nanowire interface. In contrast, the proportions of $Co^{3+}/Co^{2+}$ in NC@Fe/CoCF only reach a value of 0.98. The $Co^{3+}$ ions in the $CoO_6$ hexagonal units are generally recognized to enhance the reaction involving $O_2$, resulting in the production of oxygen intermediates. This suggests that an increased $Co^{3+}/Co^{2+}$ ratio will increase the electrocatalytic capacity [44–46]. The spectra for the Fe 2p are depicted in Fig. 2b. The presence of $Fe^0$ is indicated by two distinct peaks observed at around 707.4 and 720.0 eV, whereas the existence of $Fe^{2+}$ is confirmed by the appearance of two satellite peaks at 724.2 and 711.0 eV [47]. The introduction of $Fe^{2+}$ not only activates $H_2O_2$ to produce •OH but also alters the electronic configuration of the material, thereby enhancing its long-term stability [48]. The enhanced performance of electrocatalytic activity is attributed to the acknowledged beneficial interaction between Fe and Co ions, which has a crucial function.

The satellite Pd $3d_{5/2}$ and Pd $3d_{3/2}$ peaks were observed at 338 and 343 eV, respectively, in the Pd 3d XPS spectra (Fig. S6). The binding energy of the oxidized state is notably greater than that of metallic Pd (335 eV), providing confirmation that Pd primarily exists in the oxidized state [49]. As depicted in Fig. S7 and Table S3, the incorporation of metal doping results in an elevation of defect concentration within the carbon material, consequently enhancing the catalytic efficiency. The formation of metal-N bonds occurred upon the loading of the metal, suggesting that Pd may be coordinated to N (Fig. S8). To conduct a more in-depth examination of the atomic-level structure of Pd species, XAFS measurements were performed. The Pd K-edge XANES spectra of Pd-NC@Fe/CoCF with Pd foil and PdO references are depicted in Fig. 2c. The absorption edge of Pd-NC@Fe/CoCF is situated between that of Pd foil and PdO, indicating that the oxidation state of Pd in Pd-NC@Fe/CoCF lies between $Pd^0$ and $Pd^{2+}$. This observation aligns with the XPS findings. The FT $k^3$-weighted EXAFS spectrum of Pd-NC@Fe/CoCF in Fig. 2d exhibits a predominant peak at approximately 1.50 Å, indicating the presence of the Pd-N bond. For comparison, the Pd foil exhibits a prominent signal at 2.74 Å, indicative of Pd-Pd coordination. As depicted in Fig. 2e, the WT diagram of Pd-NC@Fe/CoCF exhibits a maximum intensity, which corresponds to a Pd-N bond. The absence of a signal related to metal bonding indicates the absence of Pd-Pd bond and Pd-$FeCo_2O_4$ bond [50,51]. The WT-EXAFS findings further support the presence of Pd in Pd-NC@Fe/CoCF as a singular atom. Consequently, it is believed that Pd atoms are dispersed atomically, as indicated by the results of HAADF-STEM and XAFS analysis. Moreover, the EXAFS fitting was performed to obtain the structural parameters and determine the precise chemical arrangement of Pd atoms (Table S4). The number of coordination bonds of the central atom Pd is approximately 3.6, and the average bond length of Pd-N is 2.32 Å. According to the data, the Pd atom is surrounded by four N atoms [52]. The analysis of Table S5 indicates that the loading of Pd SAs is approximately 1.0 wt%. Both the $FeCo_2O_4$ NWCAs and Pd SAs were effectively loaded on both the surface and the interior of the material.

The electrode exhibited significant hydrophobicity due to the presence of nanopores, particularly evident during the electrochemical process. This phenomenon is attributed to the potential filling of these nanopores by the generated $H_2$ bubble, leading to the suppression of mass and charge-transfer processes during the EHDC reaction [53]. The NC film, when loaded, serves to anchor the Pd SAs and also creates a controlled interfacial microenvironment that facilitates the smooth adsorption of contaminants and water molecules onto the reaction sites [54]. Upon loading hydrophilic NC onto the electrode, the CA value of the electrode approached 0, indicating a significant increase in hydrophilicity (Fig. S9). The alteration of the hydrophilic properties on the surface of the electrode has a direct impact on its mass transfer characteristics. To elucidate the impact of the NC layer on interfacial mass and electron transfer phenomena, we conducted a comparison of the initial electrochemical activities of Pd-Fe/CoCF, NC@Fe/CoCF, Pd-NCF, and Pd-NC@Fe/CoCF (Fig. S11). The onset potential for the hydrogen evolution reaction (HER) is approximately −0.2 V for all catalysts in neutral circumstances. This suggests the inherent HER activity of Pd-NC@Fe/CoCF may not be affected by the NC. The existence of NC had a significant impact on the current intensity, suggesting that the addition of NC effectively suppressed hydrogen evolution. The most likely explanation for the suppression of the initial HER activity of Pd-NC@Fe/CoCF by the presence of NC is that NC obstructed some of the Pd sites for the HER reaction. Additionally, the introduction of NC may have impeded the combination of two H* into an $H_2$ molecule.

### 3.2. Pulse electrocatalytic degradation of 1,2,4-TCB and TCE using Pd-NC@Fe/CoCF cathodes

Based on the unique surface properties of the Pd-NC@Fe/CoCF electrode, a low-consumption and high-efficiency square-wave pulsed electrocatalytic system was employed to effectively remove chlorinated contaminants through adsorption-enrichment-degradation [55]. When pulsed electrolysis is performed, the application of a pulsed potential on the Pd-NC@Fe/CoCF cathode leads to the occurrence of the EDL effect. This effect is responsible for regulating the absorption and release of chlorinated organic pollutants. The directional absorption/release of chlorinated organic pollutants is primarily governed by the EDL ion transport system at the interface between the electrode and electrolyte during the process of charging and discharging (Fig. 3a). In the pulsed electrocatalytic system, the transport of contaminants adheres to the adsorption-diffusion model, comprising three primary stages: (1) adsorption of chlorinated organic pollutants from the solution onto the electrode, (2) degradation of chlorinated organic pollutants at the electrode, and (3) desorption of degradation products from the electrode back into the solution [56]. In this procedure, enhancing the degradation efficiency and minimizing energy consumption can be achieved by identifying the optimal pulse parameters. As depicted in Fig. 3b and Fig. S12, the transient currents produced by the application of a peak voltage of −0.6 V were relatively small, ranging between −0.02 and 0.02 A, and the removal rate of 1,2,4-TCB was found to be low. When peak voltages of −0.7 V and −0.8 V were applied, transient currents ranging from −0.06–0.06 A were generated. Subsequently, the currents exhibited a significant increase, leading to 100 % removal rates of 1,2,4-TCB after 45 min, and the quasi-primary kinetic constants were determined to be 0.09489 $min^{-1}$ and 0.09093 $min^{-1}$, respectively. A comparison of the energy consumption revealed a value of 6.8 kWh·$kg^{-1}$, at the peak voltage of −0.7 V, while it increased to 9.2 kWh·$kg^{-1}$ at a peak voltage of −0.8 V. This phenomenon occurs because the energy consumption rises at proportion to the absolute value of voltage. When the peak voltage was decreased to −0.9 V, the current ranged between −0.04 and 0.04 A, resulting in a reduction in 1,2,4-TCB removal and a decrease in the reaction rate. The observed phenomenon can be ascribed to the high voltage of −0.9 V, which surpasses the potential for cathodic hydrogen precipitation, leading to the occurrence of a side reaction for hydrogen precipitation.

Furthermore, varying duty cycles will exert an influence on the ion atmosphere surrounding the electrode. When the duty cycle of the square wave pulse is small, the complete adsorption of pollutants is hindered, leading to occupation of the active sites on the electrode material. Conversely, when the duty cycle is large, it hinders the homogenization of pollutants in the solution. As depicted in Fig. 3c, the
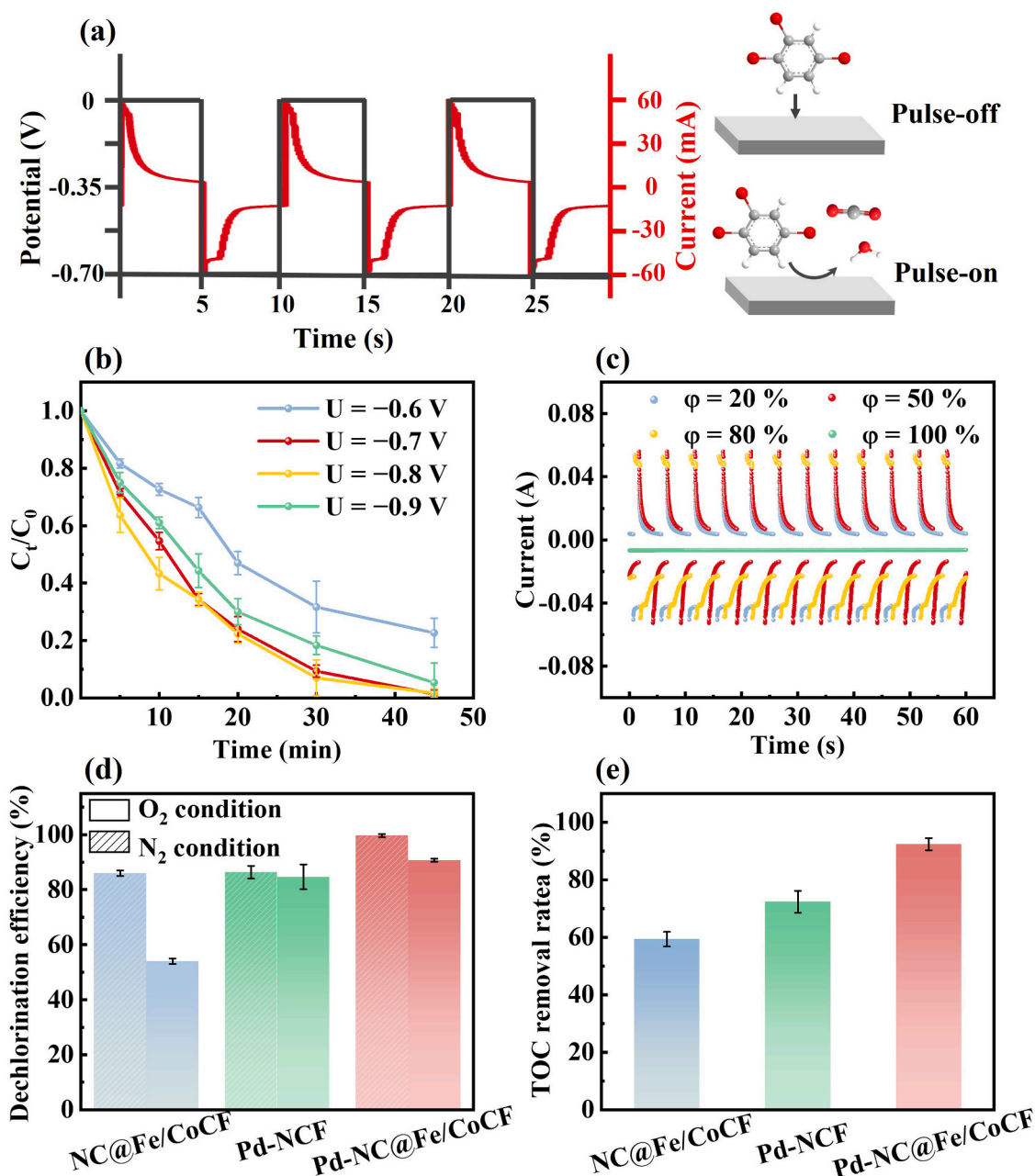
**Fig. 3.** (a) Schematic representation of the degradation of square wave pulses in 1,2,4-TCB. (b) The degradation rate of 1,2,4-TCB at various peak voltages. (c) Current curves for different duty cycles. (d) Dechlorination efficiency on different electrodes. (e) TOC removal efficiency on different electrodes.

transient current resulting from the square wave pulse voltage exhibited a notable increase in comparison to the current generated under constant voltage conditions. This phenomenon can be attributed to the adsorption of pollutants onto the electrodes, leading to the generation of a concentration gradient upon voltage activation. Additionally, the frequent desorption and release processes resulted in the supplementation of pollutants with a substantial number of ions, consequently leading to an increase in the current. As depicted in Fig. S13, when operated at a duty cycle of 20 %, the degradation rate of 1,2,4-TCB was reduced by only 80 %. The rate of removal of 1,2,4-TCB exhibited an increase with the rise in the duty cycle. At 50 % and 80 % duty cycles, the removal rate of 1,2,4-TCB approached 100 %, and the degradation effect was notably superior to that observed under constant potential voltage conditions. Upon comparison of the energy consumption, it was determined that the energy consumption at a 50 % duty cycle was approximately one-third of that at an 80 % duty cycle and about one-

fourth of that at a constant potential. Consequently, the duty cycle plays a crucial role in influencing the removal rate and energy consumption of 1,2,4-TCB within the system.

The frequency of the square wave pulse will influence the thickness of the diffusion layer during the degradation process. During the process of pulse electrolysis, it is common for pollutants to adsorb and desorb on the electrode material. As a result, the diffusion layer may not have sufficient time to fully develop, leading to a reduction in its thickness. However, at high frequencies, the duration of a single pulse cycle becomes too brief, hindering the weakening of concentration differences. Conversely, at low frequencies, the impact resembles that of conventional DC power sources, also impeding the reduction of concentration polarization [14,57,58]. Consequently, the optimal frequency is determined by the degradation experiments and is best when the degradation rate of chlorinated organics is the highest and the specific energy consumption is the lowest. As depicted in Fig. S14, the optimal degradation

rate of 1,2,4-TCB was attained when the frequency was decreased to 0.1 Hz. After comparing the energy consumption, it was determined that the frequency has less effect on the degradation process of the system. Subsequently, the parameters governing the degradation of 1,2,4-TCB in square wave pulses were further investigated using response surface methodology (Fig. S15). The obtained results were found to be in agreement with those from the one-way analysis of variance. The optimization of parameters for the degradation of square wave pulse TCE is depicted in Fig. S16. Consequently, the most suitable parameters for subsequent EF reactions are −0.7 V, 50 %, and 0.1 Hz.

Fig. S17 plots the electrochemical degradation data acquired when using different catalytic cathodes. Overall, the Pd-NC@Fe/CoCF cathode showed the highest TCE and 1,2,4-TCB degradation efficiency, such that essentially all the pollutant was decomposed after 45 min. The efficiency of TCE dechlorination during electrocatalytic reduction was determined by tracking the concentration of $Cl^-$ ions, and the findings are depicted in Fig. S18. According to theory, a $Cl^-$ concentration of 16.2 mg·$L^{-1}$ is expected to be produced from a 20 mg·$L^{-1}$ TCE and processes under $N_2$ for 45 min applying the NC@Fe/CoCF, Pd-NCF and Pd-NC@Fe/CoCF catalytic cathodes yielded chloride concentrations of 12.64, 14.26, and 15.88 mg·$L^{-1}$, respectively. The dechlorination efficiency achieved by the Pd-NC@Fe/CoCF cathode approached 100 %, whereas the NC@Fe/CoCF and Pd-NCF cathodes demonstrated efficiencies of 78 % and 88 %, respectively. Moreover, the levels of $Cl^-$ released after 45 min of degrading the 1,2,4-TCB under $N_2$ and $O_2$ are depicted in Fig. 3d. The dechlorination of the Pd-NCF, Pd-NCF, and Pd-NC@Fe/CoCF cathodes were 86 %, 87 %, and 100 %, respectively. The dechlorination efficiencies of the NC@Fe/CoCF, Pd-NCF, and Pd-NC@Fe/CoCF cathodes were 54 %, 85 %, and 91 %, respectively, after 45 min of reaction under anaerobic conditions. The NC@Fe/CoCF cathode contributed to the indirect oxidative dechlorination efficiency, while the Pd-NCF cathode was primarily responsible for the reductive dechlorination. The Pd-NC@Fe/CoCF catalytic cathode demonstrated greater effectiveness in indirect oxidative dechlorination compared to the Pd-NCF cathode. The dechlorination efficiency of the Pd-NC@Fe/CoCF catalytic cathode was 100 %. This efficiency comprised 91 % reductive dechlorination and 9 % indirect oxidative dechlorination. The complete dechlorination of 1,2,4-TCB by the Pd-NC@Fe/CoCF catalytic cathode was attributed to the synergistic effect of reductive dechlorination and indirect oxidative dechlorination.

The mineralization capabilities of various cathodes are depicted in Fig. 3e. After 45 min of electrolysis of 1,2,4-TCB using Pd-NC@Fe/CoCF, a TOC removal efficiency of 92.3 % and complete dechlorination (100 %) were observed, suggesting the complete transformation of 1,2,4-TCB into environmentally benign $CO_2$ and $H_2O$. The pH of the solution plays a crucial role in influencing the reaction rate, as depicted in Fig. S19. The degradation efficiencies of chlorinated pollutants exceeded 80 % after 45 min in the pH range of 3–11, suggesting that the electrodes can demonstrate highly effective performance in degrading chlorinated pollutants across a broad pH working range. The impact of an electrolyte concentration of 2 mmol·$L^{-1}$ $Na_2SO_4$ on the degradation of 1,2,4-TCB and TCE was examined by employing an aqueous solution containing 2 mmol·$L^{-1}$ $Na_2SO_4$ with a conductivity comparable to authentic groundwater, simulating synthetic groundwater. Similar solution conductivities may result in similar chlorinated organic pollutants removal efficiencies for real and synthetic groundwater [59]. As depicted in Fig. S20, the Pd-NC@Fe/CoCF electrode was able to exhibit excellent degradation performance of TCE and 1,2,4-TCB in 2 mmol·$L^{-1}$ $Na_2SO_4$ electrolyte. The conductivity of real groundwater is due to the presence of various anions and humid acid, so the effect on the removal of 1,2,4-TCB in different ionic and humid acid solutions was further explored. As illustrated in Fig. S21, the existence of $CO_3^{2-}$ and $HCO_3^-$ ions creates a competitive environment with the hydrogenation reaction. Additionally, the H* atoms, which are dissociated by $H_2O$, are partially utilized by $CO_3^{2-}$ and $HCO_3^-$ [60]. The adsorption sites of the electrode-humid acid complexes were found to have increased, leading

to an enhancement in the adsorption capacity. As the concentration of humid acid molecules increased, the superposition of the second humid acid layer on the first one decreased the exposure of functional groups and the adsorption sites of the complexes [37]. Furthermore, the degradation efficiency of the Pd-NC@Fe/CoCF electrode was examined for various concentrations of chlorinated organic pollutants. As illustrated in Fig. S22, the Pd-NC@Fe/CoCF electrode system demonstrated efficient removal of varying concentrations of 1,2,4-TCB and TCE, thereby validating the exceptional electrocatalytic capabilities of the Pd-NC@Fe/CoCF electrode.

The performance of the Pd-NC@Fe/CoCF electrode was evaluated through 12 consecutive pollutant degradation treatments to assess the stability and reusability of the electrode. As depicted in Fig. S23a, the degradation of chlorinated contaminants exhibited minimal change in each cycle, suggesting that the Pd-NC@Fe/CoCF electrode demonstrates exceptional reusability. Due to the "tip effect" of $FeCo_2O_4$ NWCAs (the electric field at the tip is stronger than at other locations), the impedance of the Pd-NC@Fe/CoCF electrode decreases compared to that of the Pd-NCF electrode (Fig. S23b), which indicates that the $FeCo_2O_4$ NWCAs improve the electron transfer efficiency of the material and accelerate the charge transfer. Nonetheless, the significant detachment and aggregation of nanowires resulted in a diminished impact of the "tip effect", thereby contributing to the subpar performance of the Pd-NC@Fe/CoCF electrode [61]. As depicted in Fig. S23c and Table S6, the EIS outcomes of the Pd-NC@Fe/CoCF electrode post-degradation aligned with those of the original electrode. This observation substantiates the role of the carbon film in stabilizing the $FeCo_2O_4$ NWCAs, inhibiting nanowire detachment, and preserving the "tip effect" of the electrodes. These findings confirmed the good performance of the Pd-NC@Fe/CoCF electrode. ICP-MS was employed to examine the leaching of metal ions in the reaction liquid, as depicted in Fig. S23d, indicating minimal levels. This provides additional evidence of the electrode's stability and safety when used for pollution removal.

### 3.3. Identification active species in the Pd-NC@Fe/CoCF system

Fig. 4a depicts oxidation peaks observed during positive scans, occurring between −0.20 and −0.10 V, signifying the oxidation of molecular H*. The active species H* plays a crucial role in enhancing the efficiency of hydrodechlorination due to its high reducing power [21, 62]. That is the Pd-NC@Fe/CoCF electrode favors the formation of H* (Eq. 5). The generation and utilization of H* may be clearly visible in the DPV curve within the voltage range of 0.1 V to 0 V, as depicted in Fig. 4b. As the amount of TCE increased, there was a gradual decrease in the oxidation peak of H*, indicating the utilization of H* in the hydrodechlorination process. It has also been demonstrated to reliably generate H* in a high-concentration contamination environment. To clarify the function of H* in the EHDC process, a dechlorination reaction was performed to examine the production of H* in the presence of t-BuOH, a substance utilized to suppress the function of H*. As depicted in Fig. 4c, the conversion of pollutants was evidently impeded by the rise in t-BuOH concentration. The ESR test results in Fig. 4d reveal the presence of the characteristic peak of H*. The aforementioned findings allow for the clear identification of H* generation and their respective types, as well as the observation of the trend in H* generation and consumption. This indicates the significant role of H* in the reductive dechlorination and degradation processes [19].

$$H_2O + e^- + Pd\text{-}NC@Fe/CoCF \rightarrow Pd\text{-}NC@Fe/CoCF[H]^* + OH^- \quad (5)$$

Fig. 4e illustrates the impact of reactive oxygen species removal on the degradation of 1,2,4-TCB. The inhibition of 1,2,4-TCB was observed with increasing IPA concentration. In particular, the elevation of IPA concentration to 100 mmol·$L^{-1}$ resulted in a reduction of the degradation efficiency from 100 % to 55.0 %, and a further increase to 200 mmol·$L^{-1}$ only marginally decreased the efficiency to 28.4 %. Nevertheless, the degradation of 1,2,4-TCB was not entirely impeded by
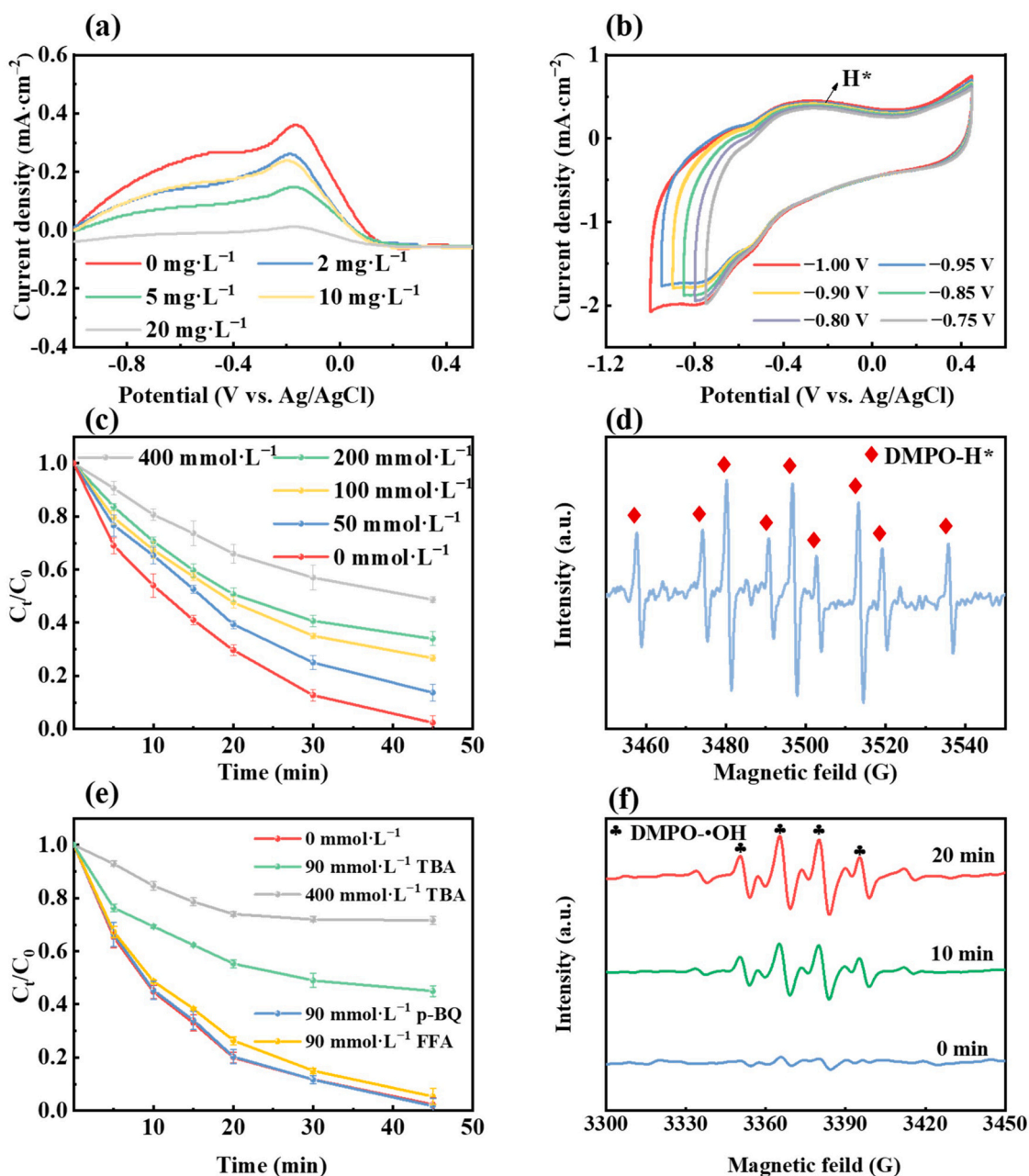
**Fig. 4.** (a) Differential pulse voltammetry test curve with ohmic-drop correction of the Pd-NC@Fe/CoCF electrode. (b) Cyclic voltammetry test curve with ohmic-drop correction. (c) Effect of quenching active hydrogen with different concentrations of t-BuOH on removal rate. (d) DMPO-H* spin trapping ESR spectra. (e) Effects of reactive oxygen species on the 1,2,4-TCB degradation. (f) Spin-trapping EPR spectra.

the presence of IPA, suggesting the involvement of additional radicals or non-radical substances in the mechanism. The inclusion of p-BQ did not impede the degradation of 1,2,4-TCB, suggesting that the involvement of $O_2^{\bullet-}$ was minimal. The addition of FFA as a scavenger of $^1O_2$ demonstrated a negligible effect. To illustrate the essential function of $\bullet$OH, EPR experiments were conducted with the inclusion of DMPO trapping. The signals for DMPO-$O_2^{\bullet-}$ and TEMP-$^1O_2$ were nearly non-existent, indicating that $O_2^{\bullet-}$ and $^1O_2$ were not active in the system [63,64]. The intensity of the DMPO-$\bullet$OH peaks exhibited a gradual increase over time and the absence of the DMPO-R peaks [65]. This observation indicates a continuous generation of $\bullet$OH and effectively rules out the possibility of false positives (Fig. 4f). As illustrated in Fig. S24, the concentrations of $\bullet$OH, $O_2^{\bullet-}$, and $^1O_2$ were 109.66 $\mu mol \cdot L^{-1}$, 7.66 $\mu mol \cdot L^{-1}$, and 10.33 $\mu mol \cdot L^{-1}$, which further demonstrated the generation of $\bullet$OH. The aforementioned findings suggest that $\bullet$OH was primarily responsible for

the breakdown of 1,2,4-TCB. Nevertheless, merely 28.4 % of 1,2,4-TCB was removed following the addition of a significant amount of IPA (200 $mmol \cdot L^{-1}$). Consequently, an electroreduction experiment was conducted on 1,2,4-TCB (Fig. 5a), resulting in a 78.0 % removal rate within a 45 min timeframe. This suggests that the degradation mechanism of 1,2,4-TCB includes the reductive dechlorination of H* and the oxidation of $\bullet$OH [20]. Meanwhile, as depicted in Fig. 5b, Pd-NC@Fe/CoCF demonstrates a higher concentration of $\bullet$OH formation compared to the other two electrode materials. In general, there is a positive correlation between the value of $C_{dl}$ and the ECSA, enabling a rough estimation of the ESCA of various electrodes. Various curves depicting the relationship between scanning speed and current density were plotted, and the CV was utilized to determine the $C_{dl}$ by examining different scanning speeds to assess the electrochemically active area. As depicted in Fig. S25, the $C_{dl}$ value of the Pd-NC@Fe/CoCF electrode
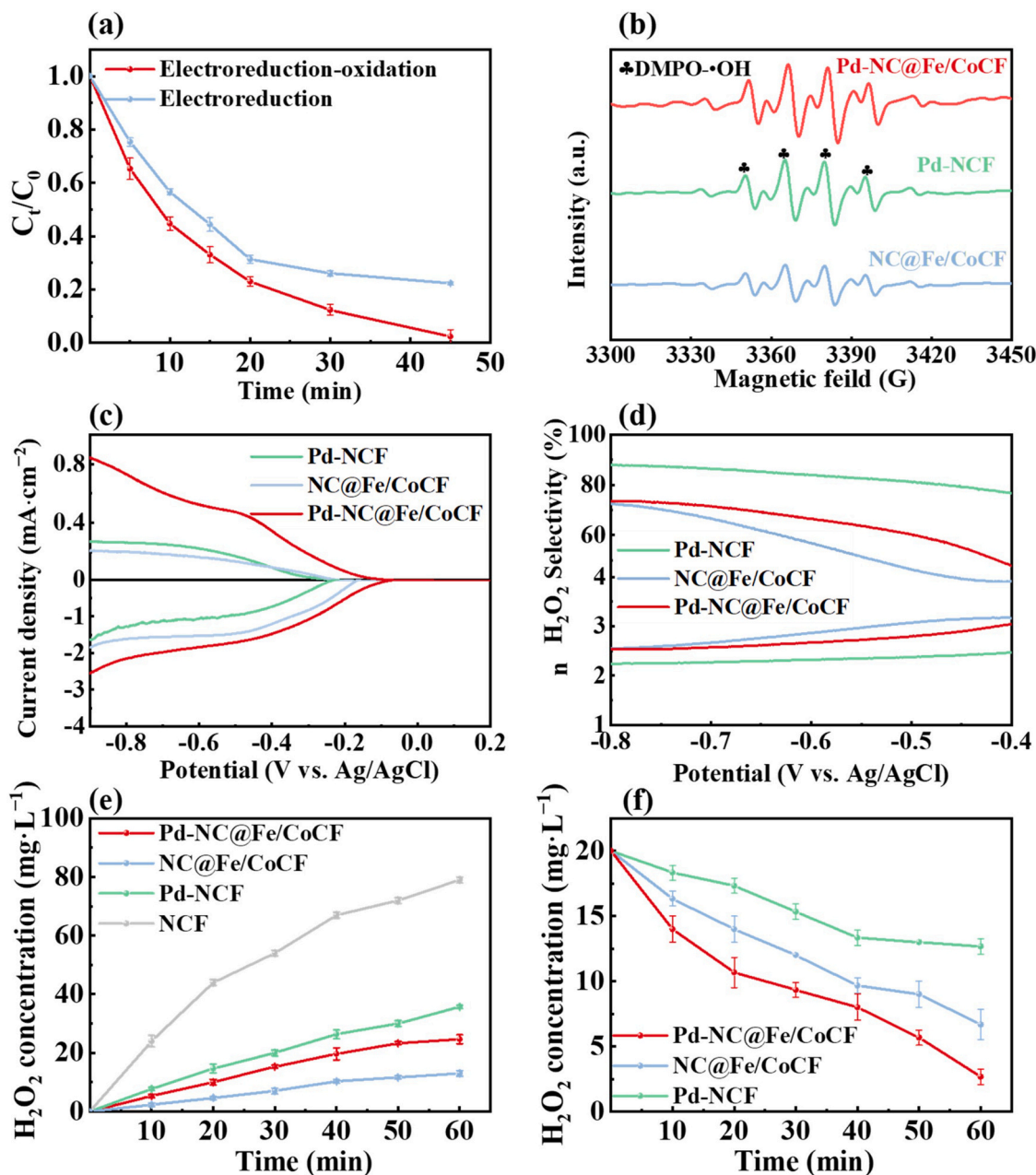
**Fig. 5.** (a) Degradation of 1,2,4-TCB by different electrochemical processes. (b) EPR spectra in different electrodes. (c) RRDE curves with ohmic-drop correction of the different catalysts in an $O_2$-saturated electrolyte at a rotation speed of 1600 rpm. (d) Electron transfer number (N) and $H_2O_2$ selectivity. (e) $H_2O_2$ production on different electrodes. (f) $H_2O_2$ decomposition experiment.

exhibited a notable increase compared to the other electrode materials, suggesting a higher potential for exposing active sites. This result further confirms the excellent electrocatalytic capability of the Pd-NC@Fe/CoCF electrode.

The investigation of the activity and selectivity of the 2e⁻ ORR involved the use of RRDE measurements. The oxygen reduction currents detected at the disk electrode and the $H_2O_2$ oxidation currents formed at the ring-disk electrode are illustrated in Fig. 5c. Upon rotating the disk and ring-disk currents, it is evident that the Pd-NCF electrode exhibits reduced ring and disk currents, while the NC@Fe/CoCF electrode demonstrates improved ORR properties attributed to the doping of $FeCo_2O_4$ NWCAs. This doping resulted in a positive shift of the onset potential by 0.06 V compared to that of the Pd-NCF electrode, but it also decreased the selectivity of 2e⁻. The Pd-NC@Fe/CoCF electrode exhibits improved ORR capabilities, leading to a positive shift in the onset

potential by 0.11 V and a significant increase in the ORR activity. Meanwhile, there was an increase in the ring current, which led to an enhancement in the selectivity for 2e⁻ ORR. The Pd-NC@Fe/CoCF electrode exhibited the highest ring and disk currents, suggesting that it possessed the highest activity and selectivity. To elucidate the electron transfer number (N) and $H_2O_2$ selectivity (%) of the NC@Fe/CoCF, Pd-NCF, and Pd-NC@Fe/CoCF electrodes. As depicted in Fig. 5d, the selectivity of the NC@Fe/CoCF, Pd-NCF, and Pd-NC@Fe/CoCF electrodes towards $H_2O_2$ was 54 %, 65 % and 82 %, respectively. The role of carbon defects formed by carbon materials and metal-specific species in the Pd-NC@Fe/CoCF electrode in promoting $H_2O_2$ generation is crucial, as indicated by the RRDE and surface property investigations. Furthermore, the activity and selectivity of the 2e⁻ ORR of the CF electrode was evaluated. As illustrated in Fig. S26, the CF electrode exhibited a minimal impact on the enhancement of $H_2O_2$ generation.

To investigate the influence of metal species and carbon defects on $2e^-$ ORR, the $H_2O_2$ yield and $H_2O_2$ decomposition of NC@Fe/CoCF, Pd-NCF, and Pd-NC@Fe/CoCF electrodes were examined in the electrochemical oxidation reaction. Defective carbon materials exhibit high $2e^-$ ORR activity and selectivity in both alkaline and neutral electrolytes [66]. As depicted in Fig. 5e, the $H_2O_2$ production of the NCF electrode exhibited a continuous increase at 1 h, with the $H_2O_2$ yield reaching 79 mg·L$^{-1}$ at 1 h, as indicated in Eq. (6). The $H_2O_2$ yields of the NC@Fe/CoCF, Pd-NCF, and Pd-NC@Fe/CoCF electrodes were relatively lower, with $H_2O_2$ yields at 1 h measured at 13.0, 35.7, and 24.3 mg·L$^{-1}$, as demonstrated in Eqs. (7)-(8). Following the RRDE and RDE findings,

the Pd-NCF exhibited greater selectivity for $2e^-$ ORR, with the $H_2O_2$ yield ranking second only to that of the NCF. As indicated in Eq. (9), the oxygen reduction at the NC@Fe/CoCF electrode resulted in the transfer of $3e^-$, and the $H_2O_2$ generated from the $2e^-$ ORR was subsequently activated to form •OH. As demonstrated in Eq. (10), the Pd-NC@Fe/CoCF electrode exhibited the greatest activity and selectivity for $2e^-$ ORR. The minimal amount of $H_2O_2$ indicated that the metal on the electrode served not only as an effective electrocatalyst but also as a catalyst for the reduction of $H_2O_2$ to •OH radicals. The produced $H_2O_2$ served as an intermediate for the Pd-NC@Fe/CoCF electrode, undergoing decomposition by the metal to generate •OH. The performance of the conversion
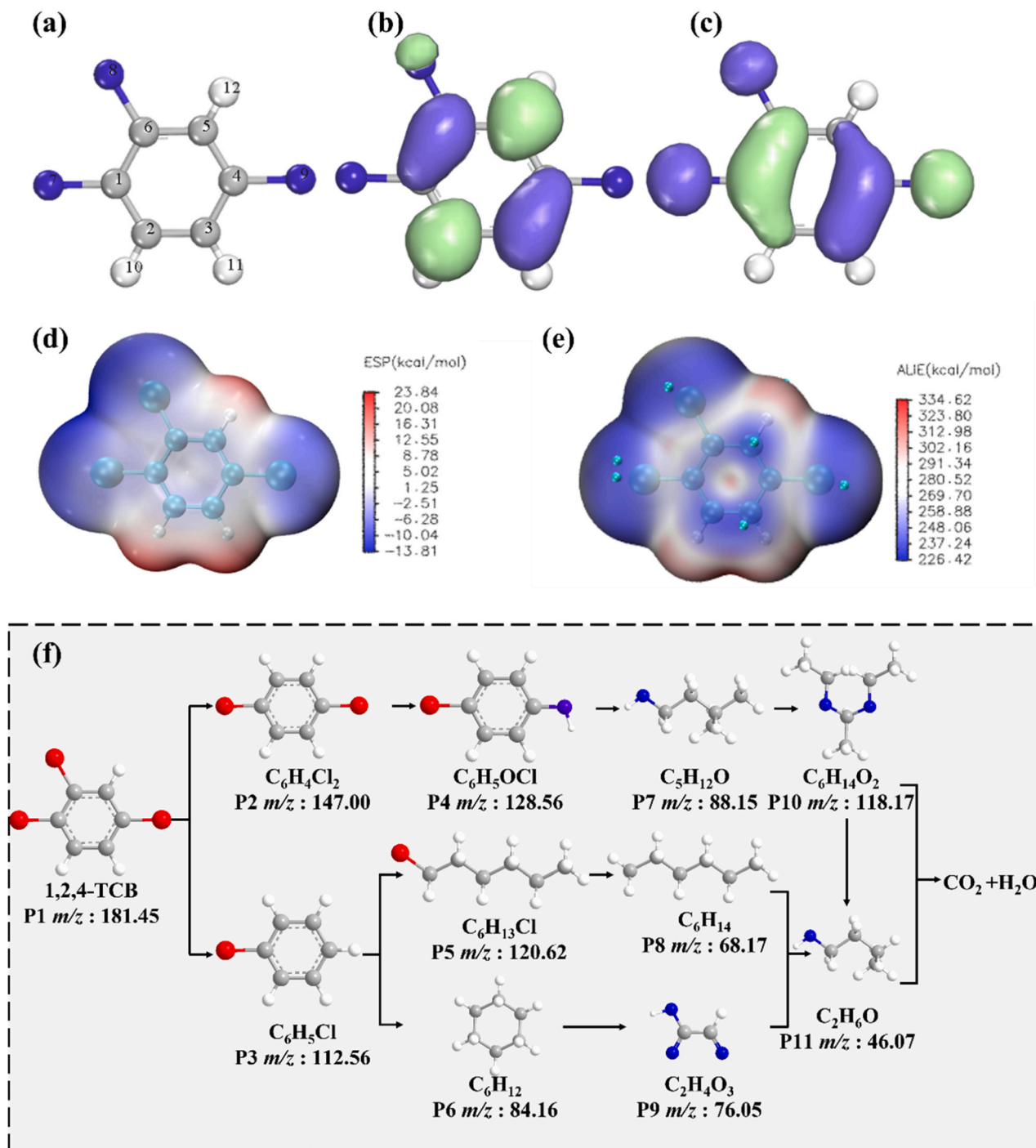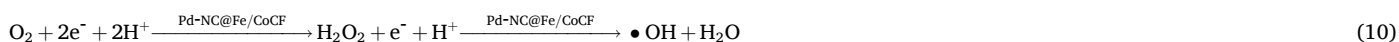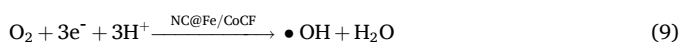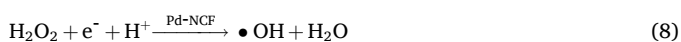


**Fig. 6.** (a) Optimal molecular structure of 1,2,4-TCB. (b) HOMO orbital. (c) LUMO orbital. (d) ESP-mapped molecular surface of 1,2,4-TCB. (e) ALIE-mapped molecular surface of 1,2,4-TCB. (f) Degradation pathway analysis of 1,2,4-TCB (reaction conditions: $C_0 = 20$ mg·L$^{-1}$, V = 50 mL, U = −0.7 V, φ = 50 %, f = 0.1 Hz).

of $H_2O_2$ to •OH was investigated through experiments testing the catalyzed $H_2O_2$ decomposition of externally supplied $H_2O_2$ reagents using NC@Fe/CoCF, Pd-NCF, and Pd-NC@Fe/CoCF electrodes. Fig. 5f illustrates that the $H_2O_2$ decomposition rate was highest at the Pd-NC@Fe/CoCF electrode, surpassing that of NC@Fe/CoCF and significantly exceeding that of Pd-NCF. This indicates that the $FeCo_2O_4$ NWCAs demonstrated a high level of $H_2O_2$ activation, leading to the production of •OH following the structure of the RRDE, RDE (Fig. S27), and $H_2O_2$ yield tests. The Pd-NCF demonstrated a high selectivity for 2e⁻ ORR, which can be attributed to the precise modulation of the coordination environment of Pd, enabling efficient capture of $O_2$ to produce $H_2O_2$. These phenomena indicate that the Pd-NC@Fe/CoCF electrode generates •OH through a two-step process of $O_2$ reduction, wherein $H_2O_2$ is generated by $O_2$ reduction on Pd-NCF, and the subsequently formed $H_2O_2$ is catalyzed to •OH by the $FeCo_2O_4$ NWCAs [67,68].

$$O_2 + 2e^- + 2H^+ \xrightarrow{\text{NCF}} H_2O_2 \tag{6}$$

$$O_2 + 2e^- + 2H^+ \xrightarrow{\text{Pd-NCF}} H_2O_2 \tag{7}$$

$$H_2O_2 + e^- + H^+ \xrightarrow{\text{Pd-NCF}} \bullet OH + H_2O \tag{8}$$

$$O_2 + 3e^- + 3H^+ \xrightarrow{\text{NC@Fe/CoCF}} \bullet OH + H_2O \tag{9}$$

electrophilic and nucleophilic reactions. Regions with more negative ESP values are generally regarded as more prone to undergoing electrophilic reactions. As depicted in Fig. 6d, the electrons are predominantly concentrated in the Cl7, Cl8, and Cl9 sites, suggesting that the electrophilic reactions primarily occur at these locations. ALIE can predict the locations of chemical reactions by analyzing the ionization energy of electrons at specified local positions. The lower the calculated value, the weaker the electron binding, the higher the activity, and the easier it is to participate in electrophilic or free radical reactions. As depicted in Fig. 6e, the values at Cl7, Cl8, and Cl9 are relatively low, indicating the likelihood of electrophilic or radical reactions occurring at these positions.

Upon examination of the GC-MS data depicted in Fig. 6f, it is evident that 1,2,4-TCB underwent gradual decomposition into chlorobenzenes, chlorophenols, alkanes, and small molecular products, ultimately resulting in mineralization to $CO_2$ and $H_2O$. Bioaccumulation factors of 1,2,4-TCB and its major degradable intermediates were further evaluated using the T.E.S.T analysis. Fig. S28 showed that the bioaccumulation factors of intermediates were significantly lower than 1,2,4-TCB [69]. From the overall results of toxicity prediction, Pd-NC@Fe/CoCF system could effectively reduce the harm and risk of 1,2,4-TCB to the overall environment. The degradation pathway was analyzed based on the GC-MS data results. As depicted in Fig. S29, the gradual dechlorination of TCE leads to the generation of DCE, followed by the rapid degradation of the formed VC, ultimately resulting in the production of ethylene.

$$O_2 + 2e^- + 2H^+ \xrightarrow{\text{Pd-NC@Fe/CoCF}} H_2O_2 + e^- + H^+ \xrightarrow{\text{Pd-NC@Fe/CoCF}} \bullet OH + H_2O \tag{10}$$

## 4. Conclusion

The investigation of pulse voltage, pulse duty cycle, and pulse frequency effects on the removal rate and energy consumption of chlorinated organic pollutants reveals that the impact of pulse voltage and pulse duty cycle on the removal rate and energy consumption is more pronounced, whereas the influence of pulse frequency is comparatively minor. Under pulsed electric field conditions, high efficiency and low consumption can be achievable with suitable pulse duty cycle conditions. Electrochemical cathodes were prepared to promote the heterogeneous electrocatalytic degradation of chlorinated organic pollutants by applying Pd SAs and $FeCo_2O_4$ NWCs. The material demonstrated the degradation of TCE and 1,2,4-TCB was conducted to examine the degradation performance and mechanism. Various experiments involving EPR, quantitative examinations, and electrochemical evaluations, have shown demonstrated that the radical H* was accountable for the degradation of TCE, while both H* and •OH radicals were responsible for the effective decomposition of 1,2,4-TCB. The Pd-NC@Fe/CoCF demonstrated a high selectivity for 2e⁻ ORR, which can be attributed to the precise modulation of the coordination environment of Pd, enabling efficient capture of $O_2$, leading to improved performance and the initiation of •OH generation from $H_2O_2$ through the 1e⁻ process. The electrocatalytic system Pd-NC@Fe/CoCF successfully achieved full dechlorination of 1,2,4-TCB within 45 min, resulting in a 92.3 % removal of TOC and demonstrating outstanding degradation of organic pollutants. This study presents a novel approach for producing highly effective multifunctional electrocatalysts to address the remediation of chlorinated organic pollutants in water.

## CRediT authorship contribution statement

**Wenchao Yu:** Methodology. **Shunlin Li:** Formal analysis. **Hui Wang:** Writing – review & editing, Supervision, Project administration,

### 3.4. Theoretical calculations and degradation mechanism

The structural properties of 1,2,4-TCB were analyzed to elucidate its removal pathway in the electrocatalytic reduction-oxidation process. The molecular structure of 1,2,4-TCB was optimized, and the optimized configuration is depicted in Fig. 6a. The boundary theory of molecular orbitals was employed to anticipate the most probable sites for molecular strike in 1,2,4-TCB. As per the molecular frontier theory, the positions of organic pollutant molecules that are likely to either lose or acquire electrons during a reaction can be determined by the HOMO and the LUMO. The HOMO orbitals represent the electron's ability to escape and are therefore associated with electrophilic processes, whereas the LUMO orbitals are associated with nucleophilic reactions. LUMO orbitals are associated with nucleophilic reactions. The reaction sites for electrophilic and nucleophilic reactions can be determined based on the HOMO and LUMO orbitals. The HOMO and LUMO orbitals of the 1,2,4-TCB molecule are depicted in Figs. 6b and 6c. In the orbital diagrams of the HOMO and LUMO, the blue color signifies the positive region, denoting a higher concentration of positively charged electrons, while the green color signifies the negative region, indicating a higher concentration of negatively charged electrons. The HOMO orbitals are predominantly situated around the Cl8, Cl9, and C2 regions, while the LUMO orbitals are primarily located on the benzene ring. This suggests that these areas are susceptible to attack by reactive species during the removal process.

The reaction sites were additionally forecasted through the computation of the ESP and ALIE, with the outcomes presented in Figs. 6d and 6e. The ESP is determined by the atomic nuclear charge and electron density, and it is intricately connected to the electronic structure. Consequently, it is frequently employed to forecast the locations of

Funding acquisition, Conceptualization. **Mengxue Li:** Writing – original draft, Visualization, Methodology, Investigation, Formal analysis, Data curation, Conceptualization. **Zhaoyong Bian:** Writing – review & editing, Supervision, Funding acquisition, Conceptualization. **Xinyu Li:** Investigation. **Xiangting Hou:** Visualization, Data curation.

## Declaration of Competing Interest

The authors declare that they have no known competing financial interests or personal relationships that could have appeared to influence the work reported in this paper.

## Data Availability

Data will be made available on request.

## Appendix A. Supporting information

Supplementary data associated with this article can be found in the online version at doi:10.1016/j.apcatb.2024.124189.

## References

[1] K. Zhao, X. Quan, Y. Su, X. Qin, S. Chen, H.T. Yu, Enhanced chlorinated pollutant degradation by the synergistic effect between dechlorination and hydroxyl radical oxidation on a bimetallic single-atom catalyst, Environ. Sci. Technol. 55 (2021) 14194–14203, https://doi.org/10.1021/acs.est.1c04943.

[2] J. Deng, F. Wu, S.X. Gao, D.D. Dionysiou, L.Z. Huang, Self-activated Ni(OH)₂ cathode for complete electrochemical reduction of trichloroethylene to ethane in low-conductivity groundwater, Appl. Catal. B Environ. 309 (2022) 121258, https://doi.org/10.1016/j.apcatb.2022.121258.

[3] C.J. Liang, C.Y. Weng, Evaluation of alkaline activated sodium persulfate sustained release rod for the removal of dissolved trichloroethylene, J. Hazard. Mater. 439 (2022) 129657, https://doi.org/10.1016/j.jhazmat.2022.129657.

[4] A. Gafni, H. Siebner, A. Bernstein, Potential for co-metabolic oxidation of TCE and evidence for its occurrence in a large-scale aquifer survey, Water Res. 171 (2020) 115431, https://doi.org/10.1016/j.watres.2019.115431.

[5] T. Durkic, J.M. Jazic, M. Watson, B. Basic, M. Prica, A. Tubic, S. Maletic, J. Agbaba, Application of UV-activated persulfate and peroxymonosulfate processes for the degradation of 1,2,3-trichlorobenzene in different water matrices, Environ. Sci. Pollut. Res. 28 (2021) 59165–59179, https://doi.org/10.1007/s11356-020-09787-w.

[6] D. Lorenzo, A. Santos, A. Sánchez-Yepes, L.Ó. Conte, C.M. Domínguez, abatement of 1,2,4-trichlorobencene by wet peroxide oxidation catalysed by goethite and enhanced by visible LED light at neutral pH, Catalysts 11 (2021) 139, https://doi.org/10.3390/catal11010139.

[7] X.W. Ma, L.J. Yang, Y. Hou, L. Zhou, Adsorption/desorption characteristics of low-concentration semi-volatile organic compounds in vapor phase on activated carbon, J. Environ. Manag. 305 (2022) 114360, https://doi.org/10.1016/j.jenvman.2021.114360.

[8] X. Shang, L. Yang, D. Ouyang, B. Zhang, W.Y. Zhang, M.Y. Gu, J. Li, M.F. Chen, L.H. Huang, L.B. Qian, Enhanced removal of 1,2,4-trichlorobenzene by modified biochar supported nanoscale zero-valent iron and palladium, Chemosphere 249 (2020) 126518, https://doi.org/10.1016/j.chemosphere.2020.126518.

[9] B. Kumar, J.P. Brian, V. Atla, S. Kumari, K.A. Bertram, R.T. White, J.M. Spurgeon, Controlling the product syngas H₂: CO ratio through pulsed-bias electrochemical reduction of CO₂ on copper, ACS Catal. 6 (2016) 4739–4745, https://doi.org/10.1021/acscatal.6b00857.

[10] Y.N. Ding, W. Zhou, J.F. Li, J.E. Wang, L. Xie, X.X. Meng, J.H. Gao, F. Sun, G.B. Zhao, Y.K. Qin, Revealing the dynamic regulation of the interfacial microenvironment induced by pulsed electrocatalysis in the oxygen reduction reaction, ACS Energy Lett. 8 (2023) 3122–3130, https://doi.org/10.1021/acsenergylett.3c00758.

[11] Y.N. Ding, L. Xie, W. Zhou, F. Sun, J.H. Gao, C.W. Yang, G.B. Zhao, Y.K. Qin, J. Ma, Pulsed electrocatalysis enables the stabilization and activation of carbon-based catalysts towards H₂O₂ production, Appl. Catal. B Environ. 316 (2022) 121688, https://doi.org/10.1016/j.apcatb.2022.121688.

[12] Y.N. Ding, W. Zhou, L. Xie, S. Chen, J.H. Gao, F. Sun, G.B. Zhao, Y.K. Qin, Pulsed electrocatalysis enables an efficient 2-electron oxygen reduction reaction for H₂O₂ production, J. Mater. Chem. A 9 (2021) 15948–15954, https://doi.org/10.1039/d1ta03864h.

[13] C. Kim, L.C. Weng, A.T. Bell, Impact of pulsed electrochemical reduction of CO₂ on the formation of C₂₊ products over Cu, ACS Catal. 10 (2020) 12403–12413, https://doi.org/10.1021/acscatal.0c02915.

[14] J. Timoshenko, A. Bergmann, C. Rettenmaier, A. Herzog, R.M. Arán-Ais, H.S. Jeon, F.T. Haase, U. Hejral, P. Grosse, S. Kühl, E.M. Davis, J. Tian, O. Magnussen, B. Roldan Cuenya, Steering the structure and selectivity of CO₂ electroreduction catalysts by potential pulses, Nat. Catal. 5 (2022) 259–267, https://doi.org/10.1038/s41929-022-00760-z.

[15] H.S. Jeon, J. Timoshenko, C. Rettenmaier, A. Herzog, A. Yoon, S.W. Chee, S. Oener, U. Hejral, F.T. Haase, B. Roldan Cuenya, Selectivity control of Cu nanocrystals in a gas-fed flow cell through CO₂ pulsed electroreduction, J. Am. Chem. Soc. 143 (2021) 7578–7587, https://doi.org/10.1021/jacs.1c03443.

[16] J.H. Wang, X.H. Long, I.Y. Zhang, R.F. Huang, Pulsed versus direct current electrochemical co-catalytic peroxymonosulfate-based system: elevated degradation and energy efficiency with enhanced oxidation mechanisms, J. Hazard. Mater. 458 (2023) 132004, https://doi.org/10.1016/j.jhazmat.2023.132004.

[17] H.Y. Zhao, L. Qian, X.H. Guan, D.L. Wu, G.H. Zhao, Continuous bulk FeCuC aerogel with ultradispersed metal nanoparticles: an efficient 3D heterogeneous electro-Fenton cathode over a wide range of pH 3-9, Environ. Sci. Technol. 50 (2016) 5225–5233, https://doi.org/10.1021/acs.est.6b00265.

[18] H. Kim, J. Lim, S. Lee, H.H. Kim, C. Lee, J. Lee, W. Choi, Spontaneous generation of H₂O₂ and hydroxyl radical through O₂ reduction on copper phosphide under ambient aqueous condition, Environ. Sci. Technol. 53 (2019) 2918–2925, https://doi.org/10.1021/acs.est.8b06353.

[19] R. Arrigo, M.E. Schuster, S. Abate, G. Giorgianni, G. Centi, S. Perathoner, S. Wrabetz, V. Pfeifer, M. Antonietti, R. Schlögl, Pd supported on carbon nitride boosts the direct hydrogen peroxide synthesis, ACS Catal. 6 (2016) 6959–6966, https://doi.org/10.1021/acscatal.6b01889.

[20] X.Q. Shen, F. Xiao, H.Y. Zhao, Y. Chen, C. Fang, R. Xiao, W.H. Chu, G.H. Zhao, In situ-formed PdFe nanoalloy and carbon defects in cathode for synergic reduction-oxidation of chlorinated pollutants in electro-Fenton process, Environ. Sci. Technol. 54 (2020) 4564–4572, https://doi.org/10.1021/acs.est.9b05896.

[21] D. Huang, D.J. Kim, D. Rigby, X. Zhou, X. Wu, A. Meese, J. Niu, E. Stavitski, J.H. Kim, Elucidating the role of single-atom Pd for electrocatalytic hydrodechlorination, Environ. Sci. Technol. 55 (2021) 13306–13316, https://doi.org/10.1021/acs.est.1c04294.

[22] Y.Y. Liu, X.J. Wang, Q.N. Sun, M. Yuan, Z.H. Sun, L.Y. Chen, Y.N. Zhang, S.Q. Xia, J.F. Zhao, Enhanced activation of peroxymonosulfate by a floating FeMo₃Oₓ/C₃N₄ photocatalyst under visible-light assistance for oxytetracycline degradation: Performance, mechanisms and comparison with H₂O₂ activation, Environ. Pollut. 316 (2023) 120668, https://doi.org/10.1016/j.envpol.2022.120668.

[23] Y.B. Zhou, Y.L. Zhang, X.M. Hu, Enhanced activation of peroxymonosulfate using oxygen vacancy-enriched FeCo₂O₄₋ₓ spinel for 2,4-dichlorophenol removal: singlet oxygen-dominated nonradical process, Colloid Surf. A 597 (2020) 124568, https://doi.org/10.1016/j.colsurfa.2020.124568.

[24] Z.M. Sun, X.R. Liu, X.B. Dong, X.W. Zhang, Y. Tan, F. Yuan, S.L. Zheng, C.Q. Li, Synergistic activation of peroxymonosulfate via in situ growth FeCo₂O₄ nanoparticles on natural rectorite: role of transition metal ions and hydroxyl groups, Chemosphere 263 (2021) 127965, https://doi.org/10.1016/j.chemosphere.2020.127965.

[25] J. Cen, P.K. Shen, Y. Zeng, Ru doping NiCoP hetero-nanowires with modulated electronic structure for efficient overall water splitting, J. Colloid Interface Sci. 610 (2022) 213–220, https://doi.org/10.1016/j.jcis.2021.12.028.

[26] M. Danish, X.G. Gu, S.G. Lu, A. Ahmad, M. Naqvi, U. Farooq, X. Zhang, X.R. Fu, Z.W. Miao, Y.F. Xue, Efficient transformation of trichloroethylene activated through sodium percarbonate using heterogeneous zeolite supported nano zero valent iron-copper bimetallic composite, Chem. Eng. J. 308 (2017) 396–407, https://doi.org/10.1016/j.cej.2016.09.051.

[27] W.T. Yu, H. Jiang, J.H. Fang, S. Song, Designing an electron-deficient Pd/NiCo₂O₄ bifunctional electrocatalyst with an enhanced hydrodechlorination activity to reduce the consumption of Pd, Environ. Sci. Technol. 55 (2021) 10087–10096, https://doi.org/10.1021/acs.est.1c01922.

[28] T. Luo, H.P. Feng, L. Tang, Y. Lu, W.W. Tang, S. Chen, J.F. Yu, Q.Q. Xie, X.L. Ouyang, Z.L. Chen, Efficient degradation of tetracycline by heterogeneous electro-Fenton process using Cu-doped Fe@Fe₂O₃: mechanism and degradation pathway, Chem. Eng. J. 382 (2020) 122970, https://doi.org/10.1016/j.cej.2019.122970.

[29] C. Liu, W. Leng, P.J. Vikesland, Controlled evaluation of the impacts of surface coatings on silver nanoparticle dissolution rates, Environ. Sci. Technol. 52 (2018) 2726–2734, https://doi.org/10.1021/acs.est.7b05622.

[30] J. Yu, Y.L. Wang, L.H. Mou, D.L. Fang, S.M. Chen, S.J. Zhang, Nature-inspired 2D-mosaic 3D-gradient mesoporous framework: bimetal oxide dual-composite strategy toward ultrastable and high-capacity lithium storage, ACS Nano 12 (2018) 2035–2047, https://doi.org/10.1021/acsnano.8b00168.

[31] Y.C. Song, H.Y. Tang, Y.J. Yan, Y.J. Guo, H. Wang, Z.Y. Bian, Combining electrokinetic treatment with modified zero-valent iron nanoparticles for rapid and thorough dechlorination of trichloroethene, Chemosphere 292 (2022) 133443, https://doi.org/10.1016/j.chemosphere.2021.133443.

[32] L. Zhang, X.Y. Zhang, C. Wei, F. Wang, H. Wang, Z.Y. Bian, Interface engineering of Z-scheme α-Fe₂O₃/g-C₃N₄ photoanode: simultaneous enhancement of charge separation and hole transportation for photoelectrocatalytic organic pollutant degradation, Chem. Eng. J. 435 (2022) 134873, https://doi.org/10.1016/j.cej.2022.134873.

[33] B. Ravel, M. Newville, ATHENA, ARTEMIS, HEPHAESTUS: data analysis for X-ray absorption spectroscopy using IFEFFIT, J. Synchrotron Radiat. 12 (2005) 537–541, https://doi.org/10.1107/S0909049505012719.

[34] F. Xiao, Z.N. Wang, J.Q. Fan, T. Majima, H.Y. Zhao, G.H. Zhao, Selective electrocatalytic reduction of oxygen to hydroxyl radicals via 3-electron pathway with FeCo alloy encapsulated carbon aerogel for fast and complete removing pollutants, Angew. Chem. Int. Ed. 60 (2021) 10375–10383, https://doi.org/10.1002/anie.202101804.

[35] Y.Y. Peng, Z.Y. Bian, W.H. Zhang, H. Wang, Identifying the key N species for electrocatalytic oxygen reduction reaction on N-doped graphene, Nano Res. 16 (2023) 6642–6651, https://doi.org/10.1007/s12274-023-5421-0.

[36] H.Y. Tang, Z.Y. Bian, Y.Y. Peng, S.L. Li, H. Wang, Stepwise dechlorination of chlorinated alkenes on an Fe-Ni/rGO/Ni foam cathode: product control by one-electron-transfer reactions, J. Hazard. Mater. 433 (2022) 128744, https://doi.org/10.1016/j.jhazmat.2022.128744.

[37] H.Y. Tang, B. Ma, Z.Y. Bian, H. Wang, Selective dechlorination degradation of chlorobenzenes by dual single-atomic Fe/Ni catalyst with M-N/M-O active sites synergistic, J. Hazard. Mater. 443 (2023) 130315, https://doi.org/10.1016/j.jhazmat.2022.130315.

[38] X.Y. Zhang, H. Wang, Y.J. Guo, S.L. Li, W.C. Yu, S.W. Xu, Z.Y. Bian, Enhanced tetracycline degradation by a confinement structure rGO/Fe₁/C₃N₄ photocathode during the sequential oxygen reduction process, Sep. Purif. Technol. 330 (2024) 125473, https://doi.org/10.1016/j.seppur.2023.125473.

[39] C. Liu, M. Zhang, H.Q. Geng, P. Zhang, Z. Zheng, Y.L. Zhou, W.W. He, NIR enhanced peroxidase-like activity of Au@CeO₂ hybrid nanozyme by plasmon-induced hot electrons and photothermal effect for bacteria killing, Appl. Catal. B Environ. 295 (2021) 120317, https://doi.org/10.1016/j.apcatb.2021.120317.

[40] Y.J. Yang, Z.Y. Bian, L. Zhang, H. Wang, Bi@BiOx(OH)y modified oxidized g-C₃N₄ photocatalytic removal of tetracycline hydrochloride with highly effective oxygen activation, J. Hazard. Mater. 427 (2022) 127866, https://doi.org/10.1016/j.jhazmat.2021.127866.

[41] S.L. Li, W.C. Yu, X.Y. Zhang, L. Liu, H. Wang, Y.Y. Peng, Z.Y. Bian, Mo-based heterogeneous interface and sulfur vacancy synergistic effect enhances the Fenton-like catalytic performance for organic pollutant degradation, ACS Appl. Mater. Interfaces 15 (2023) 1326–1338, https://doi.org/10.1021/acsami.2c19243.

[42] Q.S. Huang, B. He, W.B. Zhang, J. Wang, Y.Q. Fan, X.M. Mai, Y. Wang, Y.Y. Hou, Y. Du, P.T. Xie, F. Dang, Insights into ion occupancy manipulation of Fe-Co oxide free-standing cathodes for Li-O₂ batteries with enhanced deep charge capability and long-term capability, ACS Appl. Mater. Interfaces 12 (2020) 30268–30279, https://doi.org/10.1021/acsami.0c02087.

[43] J.F. Li, S.L. Xiong, Y.R. Liu, Z.C. Ju, Y.T. Qian, High electrochemical performance of monodisperse NiCo₂O₄ mesoporous microspheres as an anode material for Li-ion batteries, ACS Appl. Mater. Interfaces 5 (2013) 981–988, https://doi.org/10.1021/am3026294.

[44] Z.J. Liu, G.J. Wang, X.Y. Zhu, Y.Y. Wang, Y.Q. Zou, S.Q. Zang, S.Y. Wang, Optimal geometrical configuration of cobalt cations in spinel oxides to promote oxygen evolution reaction, Angew. Chem. Int. Ed. 59 (2020) 4736–4742, https://doi.org/10.1002/anie.201914245.

[45] Y.S. Liu, H. Jiang, J.Y. Hao, Y.L. Liu, H.B. Shen, W.Z. Li, J. Li, Metal-organic framework-derived reduced graphene oxide-supported ZnO/ZnCo₂O₄/C hollow nanocages as cathode catalysts for aluminum-O₂ batteries, ACS Appl. Mater. Interfaces 9 (2017) 31841–31852, https://doi.org/10.1021/acsami.7b08647.

[46] J.K. Wang, R. Gao, D. Zhou, Z.J. Chen, Z.H. Wu, G. Schumacher, Z.B. Hu, X.F. Liu, Boosting the electrocatalytic activity of Co₃O₄ nanosheets for a Li-O₂ battery through modulating inner oxygen vacancy and exterior Co³⁺/Co²⁺ ratio, ACS Catal. 7 (2017) 6533–6541, https://doi.org/10.1021/acscatal.7b02313.

[47] A. Pendashteh, J. Palma, M. Anderson, R. Marcilla, Nanostructured porous wires of iron cobaltite: novel positive electrode for high-performance hybrid energy storage devices, J. Mater. Chem. A. 3 (2015) 16849–16859, https://doi.org/10.1039/c5ta02701b.

[48] T. Grewe, X.H. Deng, H. Tüysüz, Influence of Fe doping on structure and water oxidation activity of nanocast Co₃O₄, Chem. Mater. 26 (2014) 3162–3168, https://doi.org/10.1021/cm5005888.

[49] S.J. Wei, A. Li, J.C. Liu, Z. Li, W.X. Chen, Y. Gong, Q.H. Zhang, W.C. Cheong, Y. Wang, L.R. Zheng, H. Xiao, C. Chen, D.S. Wang, Q. Peng, L. Gu, X.D. Han, J. Li, Y.D. Li, Direct observation of noble metal nanoparticles transforming to thermally stable single atoms, Nat. Nanotechnol. 13 (2018) 856–861, https://doi.org/10.1038/s41565-018-0197-9.

[50] X.C. Li, P. Shen, Y.J. Luo, Y.H. Li, Y.L. Guo, H. Zhang, K. Chu, PdFe single-atom alloy metallene for N₂ electroreduction, Angew. Chem. Int. Ed. 43 (2022) e202205923, https://doi.org/10.1002/anie.202205923.

[51] K. Saravanan, C.H. Kao, Y.C. Shao, Y.F. Wang, B.Y. Wang, H.T. Wang, C.J. Tsai, W. C. Lin, C.W. Pao, H.M. Tsai, L.Y. Jang, H.J. Lin, J.F. Lee, W.F. Pong, Magnetic anisotropic properties of Pd/Co/Pd trilayer films studied by X-ray absorption spectroscopy and magnetic circular dichroism, RSC Adv. 5 (2015) 19014–19019, https://doi.org/10.1039/C4RA15683H.

[52] G.M. Liu, Y. Huang, H.Q. Lv, H. Wang, Y.B. Zeng, M.Z. Yuan, Q.G. Meng, C. Y. Wang, Confining single-atom Pd on g-C₃N₄ with carbon vacancies towards enhanced photocatalytic NO conversion, Appl. Catal. B Environ. 284 (2021) 119683, https://doi.org/10.1016/j.apcatb.2020.119683.

[53] Z.M. Fan, H.C. Zhao, K.F. Wang, W. Ran, J.F. Sun, J.F. Liu, R. Liu, Enhancing electrocatalytic hydrodechlorination through interfacial microenvironment modulation, Environ. Sci. Technol. 57 (2023) 1499–1509, https://doi.org/10.1021/acs.est.2c07462.

[54] W.H. Zhang, Z.Y. Bian, Y.Y. Peng, H.Y. Tang, H. Wang, Dual-function oxygen vacancy of BiOBr intensifies pollutant adsorption and molecular oxygen activation to remove tetracycline hydrochloride, Chem. Eng. J. 451 (2023) 138731, https://doi.org/10.1016/j.cej.2022.138731.

[55] L.O. Conte, C.M. Dominguez, A. Checa-Fernandez, A. Santos, Vis LED photo-Fenton degradation of 1,2,4-trichlorobenzene at a neutral pH using ferrioxalate as catalyst, Int. J. Environ. Res. Public Health 19 (2022) 9733, https://doi.org/10.3390/ijerph19159733.

[56] F.F. Gao, X. Du, X.G. Hao, S.S. Li, X.W. An, M.M. Liu, M.C. Han, X.T. Wang, G. Q. Guan, An electrochemically-switched BPEI-CQD/PPy/PSS membrane for selective separation of dilute copper ions from wastewater, Chem. Eng. J. 258 (2017) 718–726, https://doi.org/10.1016/j.cej.2017.06.177.

[57] F.F. Gao, X. Du, X.G. Hao, X.L. Ma, L.T. Chang, N.C. Han, G.Q. Guan, K.Y. Tang, A novel electrical double-layer ion transport carbon-based membrane with 3D porous structure: high permselectivity for dilute zinc ion separation, Chem. Eng. J. 380 (2020) 122413, https://doi.org/10.1016/j.cej.2019.122413.

[58] P.L. Zhang, J.L. Zheng, Z.D. Wang, X. Du, F.F. Gao, X.G. Hao, G.Q. Guan, C.C. Li, S. B. Liu, An in situ potential-enhanced ion transport system based on FeHCF-PPy/PSS membrane for the removal of Ca²⁺ and Mg²⁺ from dilute aqueous solution, Ind. Eng. Chem. Res. 55 (2016) 6194–6203, https://doi.org/10.1021/acs.iecr.6b00597.

[59] J. Deng, X.M. Hu, E.L. Gao, F. Wu, W.Z. Yin, L.Z. Huang, D.D. Dionysiou, Electrochemical reductive remediation of trichloroethylene contaminated groundwater using biomimetic iron-nitrogen-doped carbon, J. Hazard. Mater. 419 (2021) 126458, https://doi.org/10.1016/j.jhazmat.2021.126458.

[60] L. Gong, N. Lv, J.L. Qi, X.J. Qiu, Y.W. Gu, F. He, Effects of non-reducible dissolved solutes on reductive dechlorination of trichloroethylene by ball milled zero valent irons, J. Hazard. Mater. 396 (2020) 122620, https://doi.org/10.1016/j.jhazmat.2020.122620.

[61] H.Y. Wang, M.Y. Yu, S.G. Cui, L.T. Dong, S.T. Wang, S. Wei, H.M. Feng, S.G. Chen, Branched CuO-Co₃O₄ nanowires coated with carbon on Cu foam for water sterilization, J. Environ. Chem. Eng. 9 (2021) 105629, https://doi.org/10.1016/j.jece.2021.105629.

[62] G.M. Jiang, M.N. Lan, Z.Y. Zhang, X.S. Lv, Z.M. Lou, X.H. Xu, F. Dong, S. Zhang, Identification of active hydrogen species on palladium nanoparticles for an enhanced electrocatalytic hydrodechlorination of 2,4-dichlorophenol in water, Environ. Sci. Technol. 51 (2017) 7599–7605, https://doi.org/10.1021/acs.est.7b01128.

[63] Y.J. Yang, Z.Y. Bian, Oxygen doping through oxidation causes the main active substance in g-C₃N₄ photocatalysis to change from holes to singlet oxygen, Sci. Total Environ. 753 (2021) 141908, https://doi.org/10.1016/j.scitotenv.2020.141908.

[64] W.H. Zhang, Y.Y. Peng, Y.J. Yang, L. Zhang, Z.Y. Bian, H. Wang, Bismuth-rich strategy intensifies the molecular oxygen activation and internal electrical field for the photocatalytic degradation of tetracycline hydrochloride, Chem. Eng. J. 430 (2022) 132963, https://doi.org/10.1016/j.cej.2021.132963.

[65] J.H. Wu, H.Q. Yu, How do metal oxides mislead spin-trapping electron paramagnetic resonance analysis? Environ. Sci. Technol. Lett. 87 (2024) 2328–8930, https://doi.org/10.1021/acs.estlett.4c00155.

[66] Q.W. Chang, P. Zhang, A.H.B. Mostaghimi, X.R. Zhao, S.R. Denny, J.H. Lee, H. P. Gao, Y. Zhang, H.L.L. Xin, S. Siahrostami, J.G.G. Chen, Z. Chen, Promoting H₂O₂ production via 2-electron oxygen reduction by coordinating partially oxidized Pd with defect carbon, Nat. Commun. 11 (2020) 2178, https://doi.org/10.1038/s41467-020-15843-3.

[67] S.L. Li, H. Wang, C.C. Qiu, J.N. Ren, Y.Y. Peng, Y. Liu, F.Y. Dong, Z.Y. Bian, Electronic structure regulation of Fe single atom coordinated nitrogen doping MoS₂ catalyst enhances the Fenton-like reaction efficient for organic pollutant control, J. Hazard. Mater. 467 (2024) 133756, https://doi.org/10.1016/j.jhazmat.2024.133756.

[68] L. Liu, Y.R. Chen, S.L. Li, W.C. Yu, X.Y. Zhang, H. Wang, J.N. Ren, Z.Y. Bian, Enhanced electrocatalytic cathodic degradation of 2,4-dichlorophenoxyacetic acid based on a synergistic effect obtained from Co single atoms and Cu nanoclusters, Appl. Catal. B Environ. 332 (2023) 122748, https://doi.org/10.1016/j.apcatb.2023.122748.

[69] X.H. Yi, H.D. Ji, C.C. Wang, Y. Li, Y.H. Li, C. Zhao, A. Wang, H.F. Fu, P. Wang, X. Zhao, W. Liu, Photocatalysis-activated SR-AOP over PDINH/MIL-88A(Fe) composites for boosted chloroquine phosphate degradation: performance, mechanism, pathway and DFT calculations, Appl. Catal. B Environ. 293 (2021) 120229, https://doi.org/10.1016/j.apcatb.2021.120229.